

MICROCOPY RESOLUTION TEST CHART
NATIONAL BUREAU OF STANDARDS-1963-A

12

NUSC Technical Report 7849
18 February 1987

Three-Dimensional Electric Field Predictions of an Iron-Copper Galvanic Couple

Rolf G. Kasper
Research and Technology Staff

DTIC
ELECTE
MAR 17 1987
S D



Naval Underwater Systems Center
Newport, Rhode Island / New London, Connecticut

Approved for public release; distribution is unlimited.

AD-A178 040

UNCLASSIFIED

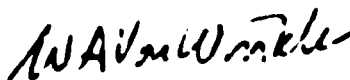
87 3 17 006

Preface

This report was prepared under Project No. A70440, "Pitting and Crevice Corrosion Kinetics," Principal Investigator Dr. R. G. Kasper (Code 101). The Sponsoring Activity is the Office of Naval Research (Code 1131M).

The Technical Reviewer for this report was Dr. R. S. Munn (Code 44).

Reviewed and Approved: 18 February 1987



W. A. Von Winkle

Associate Technical Director for Research and Technology

REPORT DOCUMENTATION PAGE

1a. REPORT SECURITY CLASSIFICATION UNCLASSIFIED			1b. RESTRICTIVE MARKINGS		
2a. SECURITY CLASSIFICATION AUTHORITY			3. DISTRIBUTION/AVAILABILITY OF REPORT Approved for public release: distribution is unlimited.		
2b. DECLASSIFICATION/DOWNGRADING SCHEDULE			5. MONITORING ORGANIZATION REPORT NUMBER(S)		
4. PERFORMING ORGANIZATION REPORT NUMBER(S) TR 7849			7a. NAME OF MONITORING ORGANIZATION Chief of Naval Research Office of Naval Research		
6a. NAME OF PERFORMING ORGANIZATION Naval Underwater Systems Center		6b. OFFICE SYMBOL (if applicable) Code 101		7b. ADDRESS (City, State, and ZIP Code) 800 No. Quincy St. Arlington, VA 22217-5000	
6c. ADDRESS (City, State, and ZIP Code) New London Laboratory New London, CT 06320			9. PROCUREMENT INSTRUMENT IDENTIFICATION NUMBER NR 036-163 (675-021X)		
8a. NAME OF FUNDING/SPONSORING ORGANIZATION Chief of Naval Research		8b. OFFICE SYMBOL (if applicable) Code 1131M		10. SOURCE OF FUNDING NUMBERS	
8c. ADDRESS (City, State, and ZIP Code) 800 No. Quincy St. Arlington, VA 22217-5000			PROGRAM ELEMENT NO. 61153N	PROJECT NO. A70440	TASK NO. RR0141-0B
			WORK UNIT ACCESSION NO. TD0140		
11. TITLE (Include Security Classification) THREE-DIMENSIONAL ELECTRIC FIELD PREDICTIONS OF AN IRON-COPPER GALVANIC COUPLE					
12. PERSONAL AUTHOR(S) Dr. Rolf G. Kasper					
13a. TYPE OF REPORT Final		13b. TIME COVERED FROM 10/85 TO 10/86		14. DATE OF REPORT (Year, Month, Day) 1987 February 18	
15. PAGE COUNT 28					
16. SUPPLEMENTARY NOTATION					
17. COSATI CODES			18. SUBJECT TERMS (Continue on reverse if necessary and identify by block number)		
FIELD	GROUP	SUB-GROUP			
07	04		Current Density Mapping		
13	10		Nonlinear Polarization		
			Numerical Analysis		
			Scanning Vibrating Electrodes		
			Three-Dimensional Electric		
			Field		
19. ABSTRACT (Continue on reverse if necessary and identify by block number) ➤ Based on completed experimental electric field scans and the corresponding finite element field predictions, it appears that the finite element numerical technique presents a strong analytical tool in calculating the nearfield electric intensity distributions about active microcells. These calculations were analytically achieved with the new double membrane finite element configuration representing nonlinear polarization and with a local tangent slope (impedance) definition dependent on the local potential difference. The experimental determination of the multidimensional current density structure was realized with a newly developed scanning vibrating electrode technique (SVET). The finite element model developed in this paper uses a priori measured uncoupled polarization curves for pure iron and pure copper. The current densities and the electric field intensities were calculated in the X, Y, and Z directions within specific regions of the					
20. DISTRIBUTION/AVAILABILITY OF ABSTRACT <input checked="" type="checkbox"/> UNCLASSIFIED/UNLIMITED <input type="checkbox"/> SAME AS RPT <input type="checkbox"/> OTC USERS			21. ABSTRACT SECURITY CLASSIFICATION UNCLASSIFIED		
22a. NAME OF RESPONSIBLE INDIVIDUAL Dr. Rolf G. Kasper			22b. TELEPHONE (Include Area Code) (203) 440-4553		22c. OFFICE SYMBOL Code 101

UNCLASSIFIED

SECURITY CLASSIFICATION OF THIS PAGE

8a. ADDRESS (Cont'd.)

Office of Naval Research

19. ABSTRACT (Cont'd.)

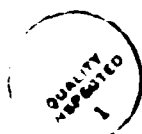
electrolyte and on its boundaries. Results appear to indicate that first-order anodic mass loss can be predicted using (1) numerically predicted current density distributions on the anodic surface and (2) Faraday's law. The electric field correlation established in this work for the three-dimensional current density components provides the confidence to proceed in the evaluation of time-dependent effects of electric fields and multipolarized surfaces associated with pitting and crevice corrosion.

UNCLASSIFIED

SECURITY CLASSIFICATION OF THIS PAGE

TABLE OF CONTENTS

	Page
LIST OF ILLUSTRATIONS	11
LIST OF TABLES	11
INTRODUCTION	1
BACKGROUND	1
ELECTROCHEMICAL MATERIALS AND MEASUREMENTS	2
EXPERIMENTAL RESULTS	6
NUMERICAL MODELING SUMMARY	10
CONCLUSIONS	13
REFERENCES	24



Accession For	
NTIS CRA&I	<input checked="" type="checkbox"/>
DTIC TAB	<input type="checkbox"/>
Unannounced	<input type="checkbox"/>
Justification	
By	
Distribution/	
Availability Codes	
Dist	Avail and/or Special
A-1	

LIST OF ILLUSTRATIONS

Figure		Page
1	A Schematic of the Iron-Copper Galvanic Couple	14
2	A Schematic of the Three-Dimensional Vibrating Probe	15
3	Arrangement of the Probe Components	16
4	The Relationship Between the X-Y-Z Specimen Coordinate System and the A-B-C Probe Drive Coordinate System	17
5	The Frequency Response of the Probe Drivers	17
6	Schematic of the Probe Tip	18
7	The Geometric Arrangement of the Three-Dimensional Scans	19
8	Potentiostatic Polarization Curves for the Iron and Copper Constituents of the Galvanic Couple	19
9	Summary of the Finite Element Model: Geometric Description, Fundamental Electrical Laws, and Boundary Conditions	20
10	Calculated and Measured J_z Components of the Ionic Current Density at 650- μm Elevation	21
11	Calculated and Measured J_z Components of the Ionic Current Density at 1125- μm Elevation (Measurement at 1150 μm)	21
12	Calculated and Measured J_R Components of the Ionic Current Density at 650- μm Elevation	22
13	Calculated and Measured J_R Components of the Ionic Current Density at 1125- μm Elevation (Measurements at 1150 μm)	22
14	Calculated and Measured Total Ionic Current Density at 650- μm Elevation	23
15	Calculated and Measured Total Ionic Current Density at 1125- μm Elevation (Measurements at 1150 μm)	23

LIST OF TABLES

Table		Page
1	Measured Ionic Current Density (pH = 1.75, σ = 42 mS/cm)	7
2	Numerical Modeling Results (Z = 650 μm , σ = 42 mS/cm)	8
3	Numerical Modeling Results (Z = 1125 μm , σ = 42 mS/cm)	8
4	Numerical Modeling Results (Z = 650 μm , σ = 62.5 mS/cm)	9
5	Numerical Modeling Results (Z = 1125 μm , σ = 62.5 mS/cm)	9

THREE-DIMENSIONAL ELECTRIC FIELD PREDICTIONS OF AN IRON-COPPER GALVANIC COUPLE

INTRODUCTION

It is generally agreed that electrogalvanic interactions of anodic and cathodic regions inherent in real world physical systems are very complex processes. This statement is particularly true in view of the highly interactive coupling that exists between multiple anodes and cathodes subject to geometric effects, inhomogeneous electrolytic mediums, polarization effects, etc. Such interactions can be characterized in a global or macroscopic sense as a complex dc electric field problem usually governed by sensitive nonlinear boundary conditions, (i.e., polarization curves for anodes and cathodes subject to the boundary conditions invariably enforced in all boundary value problems of partial differential equations). Traditionally, most of the emphasis in electrochemical research programs is focused on empirical progress to further our understanding of the various mechanisms. Often, therefore, galvanic series charts oversimplify the interactions between a variety of metals and alloys and thus are inadequate and misleading in terms of predicting detailed corrosion behavior.

A quantitative attempt to understand these complex electrolytic mechanisms was made some 40 years ago with the introduction and description of mixed-potential theory.¹ This theory states that any electrochemical reaction can be divided into one or more oxidation reactions and one or more reduction reactions. It further asserts that there exists no net charge accumulation during an electrochemical reaction. This is, of course, an expression of conservation of charge. The significance of these statements is in the recognition that electrically coupled metals in an electrolyte behave totally differently from the same metals when they are electrically isolated. Hence, the observed synergism between the more dominant variables needs to be somehow mathematically integrated into the total solution process.

BACKGROUND

The traditional method of determining adequate cathodic protection for a physical system is generally based on experience and extremely crude guidelines. Past analytical attempts to calculate local current distributions in the anodic/cathodic neighborhood (surfaces) generated immediate realizations that exact mathematical solutions seemed intractable.² It appeared that any closed form mathematical attempts would be restricted to simplified geometric electrochemical sources. Various theoretical treatments were published in the 1950's by Wagner^{3,4} and by Weber,⁵⁻⁷ addressing coplanar electrode configurations with varying degrees of polarization effects. These analyses were generally limited to one-dimensional efforts in Cartesian coordinate systems with simplified polarization mechanisms. A mathematical analysis of circular corrosion

cells with unequal polarization parameters⁸ demonstrated the treatment of slightly more complex geometry in the presence of more realistic polarization effects.

In recent years, mathematical models have been developed that apply finite element numerical techniques to the prediction of macroscopic electrogalvanic fields. These models were developed for performance predictions of cathodically protected structures, particularly in the marine and nuclear-cooling environments.⁹⁻¹⁴ Although the models did not consider changes in geometry and electrolyte properties, they were considered quite successful in predicting current distributions at the various anodic and cathodic areas of large-scale structures. Furthermore, improvements in defining nonlinear, gradient-dependent boundary conditions at electrode surfaces have provided significant progress in addressing complex polarization.^{15,16}

More recent advances in techniques for measuring localized currents in solutions have introduced methods for measuring ionic currents associated with corrosion microcells. The new techniques use vibrating probes to measure currents in a solution with spatial and current density resolutions on the order of 15-20 μm and 5 nA/cm^2 , respectively.¹⁷ Thus, it is possible to measure corrosion currents resulting from individual local cell activity on a scale close to the size of many microstructural features of materials. This technique is particularly useful for studies of localized corrosion phenomena, such as pitting and crevice corrosion, and for studies of corrosion in composite materials where local galvanic effects between constituents and interfaces may be important.^{18,19}

Progress in the finite element method for predicting one-dimensional electrogalvanic fields using data from a one-dimensional scanning vibrating electrode technique (SVET) was documented by Kasper and Crowe.²⁰ The model that was constructed provides for nonlinear polarization effects and the possibility that these polarization effects will evolve with time. The results demonstrated the steady-state capabilities of the model, as well as the need to resolve the true three-dimensional nature of the local electric field density. The uniqueness of this work is that the electrochemical measurements needed to verify calculated vector components of an electrogalvanic field predicted by the finite element method were made. These measurements were taken in one- and three-dimensional spatial configurations.

The mathematical treatment in this report addresses the true nonlinear aspects of the polarization of the anode and the cathode surface areas. The measured electrode polarizations become, in effect, nonlinear impedance relationships that are functions of the local potential; i.e., the vector constitutive equation becomes nonlinear.

ELECTROCHEMICAL MATERIALS AND MEASUREMENTS

A galvanic couple was constructed of 6.35-mm-diameter Marz grade iron and 50.8-mm-diameter Marz grade copper obtained from MRC, Inc., Orange, New Jersey. The iron anode was press fit into a centrally located hole in the

copper cathode to produce a cylindrically symmetrical planar galvanic couple, as shown in figure 1. The couple was metallographically polished using standard techniques, with 1.0- μ m diamond paste providing the final finish. Individual specimens for polarization measurements were produced from the same materials, and all were thoroughly cleaned in ethanol before testing.

Electrochemical tests were conducted in open cells in laboratory air. All electrochemical measurements were made using 0.6 M NaCl electrolytes prepared with reagent grade chemicals and distilled water. The pH was adjusted to 1.75 with HCl. The measured solution conductivity, σ , was 63 mS/cm at pH = 1.75.

The standard potentiostatic polarization response of the constituent materials was measured. The specimens for these tests were machined from the same copper and iron rods used to construct the galvanic couple. Polarizations were performed using a PAR model 173 potentiostat in combination with a PAR model 175 universal programmer at a stepping rate of 0.1 mV/s. Standard ASTM G5-78 procedures were used.

Ionic current density measurements were performed using the three-dimensional vibrating probe instrument shown schematically in figure 2. This instrument was designed and built by E and B Systems, Nashville, Tennessee. It has six major components: the microcomputer, the drive heads and amplifiers, the microelectrodes, the microelectrode preamplifier, and two constant current sources.

The IBM-PC microcomputer provides instrument control, data acquisition, signal processing, and display and storage functions. Instrument control and data acquisition are accomplished by computer interface to a Tekmar Lab Master AD/DA converter. In addition to controlling the motion of the vibrating probe and the measurement currents, the computer and interactive software provide for calibration of the system, measurement of the electrode impedance, and data analysis and output.

The drive heads consist of three electromagnetic drivers, which are connected to the measuring microelectrode by 3-mm mylar tubes arranged in such a fashion that the three orthogonal drives axes form a cube (figure 3). The diagonal of the cube is positioned vertically. Each driver consists of a modified permanent-magnet loudspeaker, which vibrates the measuring microelectrode through the mylar tubes using a push-pull motion. The drivers respond to sinusoidal signals generated in the microcomputer. These signals are applied to the drive heads through the driver amplifiers, resulting in a circular motion of the probe tip in a plane angled at 54.7 degrees to the axis of the probe. The relationship between the X-Y-Z specimen coordinate system and the A-B-C probe drive coordinate system is shown in figure 4. The frequency response of the drivers is shown in figure 5. As can be seen, the drivers provide adequate displacements for measurement of the current density at off-resonance frequencies. In contrast, the piezoelectric drivers used in one-dimensional probes lose their stroke rapidly when operated off-resonance.

The microelectrode system consists of two electrodes: the measuring electrode and the reference electrode. The measuring electrode is a

platinized, gold-plated, tungsten wire electrode, which is insulated with paralene. It is mounted in the junction of the mylar drive tubes, with the tip of the probe exposed, as shown in figure 6. The reference electrode is a silver/silver chloride electrode rigidly attached to the preamplifier. The preamplifier contains a two-stage differential preamplifier, which provides a gain of 10^4 in the voltage difference between the vibrating measuring electrode and the reference electrode.

The theoretical sensitivity limit of the electrode is determined by the electrode impedance and thermal noise of the electrode. The exposed area of the electrode tip determines both its spatial resolution and impedance. Thus, tip preparation is important.

When the electrode area is small, as required for fine spatial resolution, the resistive component of the electrode impedance is high, causing an appreciable noise level. This electrode impedance depends upon both the electrode area and the frequency of vibration. The relationship between these parameters is given by Geddes as approximately²¹

$$Z = \frac{0.225 \times 10^{14}}{kaf^{(1-\alpha)}} \quad (1)$$

where Z is the electrode impedance, k is a constant that depends on the type and condition of the electrode, a is the electrode area (in μm^2), f is the frequency of vibration, and α is a constant that relates the rate at which the electrode capacitance, c , decreases with frequency (i.e., $c = kf^{-\alpha}$). The electrode impedance, measured before each run, was typically 1 to $1.5 \times 10^5 \Omega$ at 1.5 kHz and 5 to $6 \times 10^5 \Omega$ at 300 Hz.

The ability of the electrode to efficiently detect the electric field depends upon the noise level of the electrode and the amplification of the signal. Electrode noise arises from the random movement of charge carriers at the electrode/electrolyte interface as the electrode establishes and maintains equilibrium with the electrolyte or as the electrode responds to the passage of current. This random movement of charge carriers creates a resistive component to the electrode impedance, which becomes the noise generator. The noise voltage is generated at all frequencies and is given by the relation

$$E = [4kTR(f_h - f_l)]^{0.5} \quad (2)$$

In this relation, E is the root-mean-square noise voltage, k is Boltzmann's constant, T is the absolute temperature, R is the universal gas constant, and f_h and f_l are the upper and lower cutoff frequencies of the measuring system (or the bandwidth).

To minimize the noise, it is necessary to have as narrow a bandwidth as possible. An ultra-narrow bandwidth is obtained during data reduction using the ultra-narrowband phase coherent filtering algorithm.²¹ This algorithm allows the gradients, as well as the current density components, to be

extracted from the data measured during rotation of the electrode in a circle. The measured voltages from the rotating electrode are represented by a Taylor-series expansion about the central point (A_0, B_0) of the circle of radius r swept out during rotation through angle θ of the probe tip. Thus,

$$\begin{aligned}\phi(A, B) &= \phi(A_0, B_0) + \frac{\partial \phi}{\partial A} \bigg|_{(A_0, B_0)} (A - A_0) + \frac{\partial \phi}{\partial B} \bigg|_{(A_0, B_0)} (B - B_0) \\ &= \phi(A_0, B_0) + r \cos \theta \frac{\partial \phi}{\partial A} \bigg|_{(A_0, B_0)} + r \sin \theta \frac{\partial \phi}{\partial B} \bigg|_{(A_0, B_0)},\end{aligned}\tag{3}$$

where $(A - A_0) = r \cos \theta$, $(B - B_0) = r \sin \theta$, and the partial derivatives are evaluated at (A_0, B_0) . The current density at the central point (A_0, B_0) has components J_A and J_B given by the convolution integrals

$$J_A = -\frac{\sigma}{r} \int_0^{2\pi} V(\theta) \cos \theta \, d\theta$$

and (4)

$$J_B = -\frac{\sigma}{r} \int_0^{2\pi} V(\theta) \sin \theta \, d\theta,$$

where $V(\theta)$ is the measured voltage at rotation angle θ and σ is the conductivity of the electrolyte at (A_0, B_0) . Use of this procedure allows current densities of 5 nA/cm² to be detected.

In operation, the computer feeds sinusoidal driving signals to the drive heads, in sequence, two at a time, so that the probe tip is forced to rotate in circles in the three orthogonal planes angled at 54.7 degrees to the probe axis. The diameter of the circle is adjusted as an experimental variable. The differential voltage is then sampled at 256 points around the circumference of each circle. These data are averaged over 1000 cycles or more and then stored in the computer for analysis.

During analysis the microcomputer evaluates the convolution integrals for 1000 or more cycles of the probe rotation, adjusts for orientation relative to the sample, averages the current densities, and calculates the gradients.

As each of the combinations of drives is energized in sequence, a three-dimensional volume of electrolyte is sampled and a redundant set of the components of the current density vector and gradients is obtained. Transformation of coordinate systems from the A-B-C to the X-Y-Z system is performed in the computer, displayed on the computer monitor, and stored in ASCII files on the disks for future analysis.

Calibration of the probe is accomplished by measuring a known uniform current density field in an electrolyte contained in a separate calibration dish, which is mounted on a turntable. The field is rotated through 12 standard positions, 30 degrees apart. At each position, the output voltage is measured when a single drive is energized. This technique allows the average line of motion of the electrode in the horizontal plane to be determined for that drive, as well as the mechanical lag between the drive voltage and the mechanical response of the probe. Appropriate mathematical calculations of these data provide an exact description of the probe motion and the measured values of the known field from which calibration factors are extracted and stored for data reduction.

Mechanical positioning of the probe in the X-Y plane parallel to the specimen surface is achieved using two Klinger model MT-160 stepping motor-driven translation stages mounted at right angles. These translation stages allow indexing of the specimen relative to the probe in 1- μm increments to an average accuracy of 2 μm . Control of the stages is achieved either manually or by computer using a Klinger model CC-1 universal programmable indexer.

For the experiments reported here, the vibration probe tip was positioned above the surface of the iron-copper galvanic couple at either 650- or 1150- μm elevation and current density measurements were made. The arrangement, which is shown schematically in figure 7, was designed so that the three-dimensional probe measurements were directly comparable with the one-dimensional measurements reported earlier.²⁰ At each elevation, a single line scan was performed so that the probe tip traveled parallel to a line passing through the center of the galvanic couple.

EXPERIMENTAL RESULTS

The anodic and cathodic potentiostatic polarization curves for the uncoupled iron and copper (Fe-Cu) in 0.6 M NaCl at a pH level of 1.75 and a temperature of 25° C are shown in figure 8. These polarization characteristics were reflected in the experimental setup, as well as in the impedance-controlled boundary conditions of the finite element model.

The components of the measured ionic current density vectors, in polar coordinates, as a function of position, are listed in table 1.

Numerical calculations were performed using the finite element model developed in reference 20 and summarized in figure 9. This finite element model contains (1) a geometric description of the galvanic couple and the electrolyte (figure 9(a)), (2) the fundamental electrical laws that govern the behavior of the galvanic couple in partial differential equation form (figure 9(b)), and (3) the associated Neumann boundary conditions (figure 9(c)). The numerically predicted values for J_r and J_z are listed in tables 2 and 3 for assumed electrolyte conductivities of 42 mS/cm and in tables 4 and 5 for conductivities of 62.5 mS/cm. Figure 10 shows the calculated and measured J_z ionic current density component as a function of radial position at 650 μm above the electrode surface. Figure 11 shows

Table 1. Measured Ionic Current Density
(pH = 1.75, $\sigma = 42 \text{ mS/cm}$)

Radius (mm)	Height (μm)	J_Z (A/m^2)	J_R (A/m^2)	J Total (A/m^2)
0	650	14.300	5.430	15.296
1	650	8.420	12.250	14.865
2	650	4.400	11.210	12.043
3	650	2.350	9.320	9.612
5	650	0.225	5.350	5.355
7	650	-0.100	2.790	2.792
9	650	-0.044	2.030	2.030
11	650	-0.139	1.670	1.676
13	650	0.007	1.500	1.500
15	650	-0.068	1.370	1.372
17	650	-0.162	1.310	1.320
19	650	0.005	1.180	1.180
21	650	-0.009	1.090	1.090
23	650	-0.142	0.990	1.000
25	650	-0.007	0.710	0.710
0	1150	6.910	2.960	7.517
1	1150	3.520	4.320	5.573
2	1150	2.310	4.480	5.040
3	1150	1.660	4.250	4.563
4	1150	0.858	3.980	4.071
6	1150	0.407	3.070	3.097
8	1150	0.111	1.650	1.654
10	1150	0.608	1.050	1.213
12	1150	0.061	1.120	1.122
14	1150	0.049	0.940	0.941
16	1150	-0.008	0.940	0.940
18	1150	-0.050	0.950	0.951
20	1150	0.071	0.840	0.843
22	1150	-0.004	0.800	0.800
24	1150	0.051	0.770	0.772
0	650	14.300	5.430	15.296
0	1150	6.910	2.960	7.517
0	1650	5.290	7.080	8.830
0	2150	4.360	1.850	4.730

Table 2. Numerical Modeling Results
($Z = 650 \mu\text{m}$, $\sigma = 42 \text{ mS/cm}$)

Radius (mm)	J_R (A/m ²)	J_Z (A/m ²)	J Total (A/m ²)
0.7	+2.414	10.57	10.842
1.786	3.7582	7.4759	8.367
2.778	3.6514	4.8028	6.033
4.375	3.3654	2.5709	4.235
5.897	2.6823	0.93195	2.839
7.713	1.5649	0.0633	1.566
9.73	0.98767	0.1707	1.002
11.29	0.689	0.1820	0.7126
13.875	0.44	0.1975	0.4822
17.125	0.2558	0.2232	0.33948
20.375	0.1185	0.2239	0.2533
23.65	0.03638	0.15278	0.15705

Table 3. Numerical Modeling Results
($Z = 1125 \mu\text{m}$, $\sigma = 42 \text{ mS/cm}$)

Radius (mm)	J_R (A/m ²)	J_Z (A/m ²)	J Total (A/m ²)
0.7	1.497	7.596	7.742
1.786	2.967	5.989	6.684
2.778	2.9182	4.1926	4.726
4.375	2.894	2.293	3.692
5.897	2.3986	0.9784	2.591
7.713	1.486	0.10215	1.4895
9.73	0.96688	0.10625	1.002
11.29	0.6828	1.7137-1	0.7039
13.875	0.436	0.19835	0.479
17.125	0.25559	0.20559	0.328
20.375	0.1195	0.202514	0.235
23.65	0.1641	0.13939	0.215

Table 4. Numerical Modeling Results
($Z = 650 \mu\text{m}$, $\sigma = 62.5 \text{ mS/cm}$)

Radius (mm)	J_{R2} (A/m ²)	J_Z (A/m ²)	J Total (A/m ²)
0.7	5.039	15.99	16.765
1.786	6.833	8.2107	10.682
2.778	4.8525	2.46	5.44
4.375	2.593	0.6134	2.664
5.897	1.33	0.0568	1.33
7.713	0.8353	0.07133	0.83836
9.73	0.55485	0.010757	0.56518
11.29	0.3961	0.10948	0.406
13.875	0.2557	0.11634	0.2809
17.125	0.1507	0.1316	0.19959
20.375	0.070059	0.1308	0.14835
23.65	0.020349	0.0885	0.0908

Table 5. Numerical Modeling Results
($Z = 1125 \mu\text{m}$, $\sigma = 62.5 \text{ mS/cm}$)

Radius (mm)	J_{R2} (A/m ²)	J_Z (A/m ²)	J Total (A/m ²)
0.7	3.0225	10.1026	10.545
1.786	5.1936	6.406	6.246
2.778	3.8138	2.722	4.685
4.375	2.3307	0.813686	2.468
5.897	1.323	0.1998	1.338
7.713	0.8142	0.1831	0.8345
9.73	0.5468	0.081539	0.5528
11.29	0.3931	0.1088	0.4078
13.875	0.2544	0.12016	0.2813
17.125	0.15058	0.1226	0.194
20.375	0.07069	0.12016	0.139
23.65	0.009918	0.08258	0.083

a comparison of the measurements at $Z = 1150 \text{ } \mu\text{m}$ with the calculated results at $Z = 1125 \text{ } \mu\text{m}$. The agreement between the measurements using the one-dimensional (1-D) probe (small insert in figure 11) is excellent, and both sets of measurements are in excellent agreement with the finite element model calculations. As can be seen in these figures, the anodic current density normal to the couple is highest near the center of the iron. The normal current density falls rapidly to a low value just past the iron-copper interface, and there is a dispersion in J as the elevation above the surface increases.

Figure 12 shows the measurements of J_R obtained using the three-dimensional probe compared with the finite element calculations at $Z = 650 \text{ } \mu\text{m}$. It should be pointed out that the measured components of $J(J_x, J_y, J_z)$ were changed to a set of J_R and J_z components to compare with the finite element results. The X and Y components of J were squared, and the square root of the sum of the squares resulted in J_R . This change allowed a clearer point-to-point comparison between theory and measurement. (Tables 1 through 5 already include this information.) The measured results at $1150 \text{ } \mu\text{m}$ are shown compared with the finite element calculations at $1125 \text{ } \mu\text{m}$ in figure 13. Since the one-dimensional probe cannot measure these components of the current density vector, there are no comparable one-dimensional measurements. Again, the agreement between the measurements and the calculations is excellent.

Figures 14 and 15 show the measured and calculated total current density versus radial distance at $Z = 650 \text{ } \mu\text{m}$, respectively. The ionic currents flowing from the iron are readily discernible. The finite element values and the measured values from the three-dimensional probe are plotted in figures 11 through 15. The iron-copper interface is located at a radial distance of 3.175 mm from the center. The measured values from the second scan at $1150 \text{ } \mu\text{m}$ above the electrode surface, as well as the finite element results at $1125 \text{ } \mu\text{m}$ above the electrode surface, show excellent correlation. At both elevations, it appears that the current density emanating from the anode surface is quite high, with a fairly evenly distributed current density response on the copper surface. The total calculated current leaving the anodic surface was $+2.857612 \times 10^{-5} \text{ A}$, and the total current arriving over the copper surface was $-2.857670 \times 10^{-5} \text{ A}$. This highly accurate match in magnitude between the anodic and cathodic currents illustrates the accuracy of the current-accounting system in the model.

NUMERICAL MODELING SUMMARY

An extensive discussion of the numerical procedures for the three-dimensional finite element model illustrated in figure 9 has already been presented by Kasper and Crowe.²⁰ With the emphasis here on the spatial comparison of current density vectors in cylindrical coordinates very near the electrode surfaces, it is important that several aspects of the mathematical procedures be discussed because of the sensitivity of the current density vector field response to nonlinear polarization effects, choices of interpolation functions, manner of discretization, geometry, etc. The introduction of the double nonlinear convective film membrane to

represent the nonlinear polarization of iron and copper is fully discussed elsewhere.¹⁵

Yet, some discussion on the finite element modeling subtleties is essential. The finite element model developed for this investigation was constructed from three-dimensional elements using the COSMIC/NASTRAN* program. Because three-dimensional finite elements are more difficult to implement, careful numerical tracking for accuracy and consistency is required to develop numerical confidence. The results reported here provide a first step in exercising the model for three-dimensions. Before their presentation, however, it is worthwhile to discuss several aspects of the model and the resulting computations.

First, the electrolyte was represented with CHEXA2 and CWEDGE elements. The CHEXA2 element is a three-dimensional solid, with eight vertexes and six quadrilateral faces, that is represented by two overlapping tetrahedra. The CWEDGE element is a three-dimensional solid with three quadrilateral faces and two opposing triangular faces. These elements use linear interpolation functions for the potential between adjacent grid points. The general geometric configurations of the electrolyte and the anodic/cathodic surfaces have been illustrated in figure 10.

The model was bounded by the following cylindrical coordinates: $0.0 < R < 0.044$ m, $0^\circ < \theta < 36^\circ$, and $0.0 < Z < 0.0095$ m. The selection of the 36-degree wedge angle was governed mainly by the choice of the CWEDGE and CHEXA2 elements and the anodic area in such a way that the total number of three-dimensional elements would be reasonable for computational purposes (figure 9(a)). The aspect ratios for the elements appeared reasonable, although somewhat greater discretization in the radial direction (especially in the anodic area) would have been more desirable. On all surfaces of the model, the normal derivative of the potential function was assumed to be zero (insulated). This assumption includes the surfaces $\theta = 0^\circ$ and $\theta = 36^\circ$ where the normal derivative is the θ direction.

The idea of dealing with a geometric singularity, such as a pit or a crevice, appeared to rule out the possibility of using any axisymmetric finite elements. Even though similar techniques, when applied to axisymmetric problems, appeared to provide reasonable results, axisymmetric finite elements are not adequate in addressing the geometric changes of pits or crevices evolving with time. Therefore, it was necessary to introduce the three-dimensional elements that would ultimately be required to address general pitting and crevice corrosion.

Furthermore, if three-dimensional elements such as CWEDGE and CHEXA2 were used in model development, the question of whether these elements are mathematically accurate enough to capture the various potential gradient changes, especially near the iron electrode, required attention. The CWEDGE and CHEXA2 elements use linear interpolation functions in such a way that

*NASTRAN is an acronym for the National Aeronautics and Space Administration Structural Analysis Computer Program. COSMIC/NASTRAN indicates that it is a Government-proprietary NASTRAN code.

the potential is expressed as a linear algebraic equation in R , θ , and Z . Another advantage is that these three-dimensional elements do not suffer from singularity problems because of the local formulation of the interpolation function. As constructed, the model provides the continuous variation of ϕ as a function of Z at $R = 0$.

Finally, it was desirable to attempt to control the current flow through the polarization layers by introducing surface-dependent nonlinear current-potential relationships (polarization curves), as shown in figure 9(c). (It is anticipated that these polarization curves may vary with time.) The current flow problem across the electrode-electrolytic interface appears to be conveniently modeled using convection elements instead of conduction elements.¹⁵ Like the convection boundary problem in thermal science, the determining factors for electrode performance are surface area, film resistance location, and local potential difference. The boundary conditions on the electrode surfaces are constructed by assigning the anodic and cathodic potential in the interfaces to the uncoupled open-circuit corrosion potentials of the constituents. As depicted in figure 9(c), two nonlinear film elements (CHBDY) are connected to the electrolyte. The bottom film elements are bounded by the measured open-circuit potentials for the anodic and cathodic surfaces physically described in figure 8.^{15,20}

An additional requirement imposed on the model is that the divergence of the current density vector, J , must be equal to zero. In this investigation, special adjustments were made to the COSMIC/NASTRAN finite element program to fulfill this condition. The COSMIC/NASTRAN program and related postprocessing program are resident on a VAX-11/780 computer at the Naval Underwater Systems Center in New London, Connecticut.

A number of planes were identified in order to more easily retrieve current densities and voltage information from the elements and grid points, respectively. Because the measurements for the current density were performed at 650 and 1150 μm above the electrode surfaces, it was desirable to obtain calculated current density information at the centroids of the associated elements. The lowest plane was assumed to exist at $Z = 0$. The centroid for the elements coincides with the elevation of the measured values ($Z = 650 \mu\text{m}$). Similarly, the other elements from the finite element model have a centroidal vertical distance of $Z = 1125 \mu\text{m}$, while the experimental elevation value was 1150 μm . The topmost plane (electrolyte/air interface) is located at $Z = 9500 \mu\text{m}$.

It was determined in the course of the analysis that the current density of the θ direction was indeed zero normal to the $R - Z$ planes for $\theta = 0^\circ$ and $\theta = 36^\circ$. Thus, the boundary conditions were satisfied. Over the entire $\Delta\theta$ slice, the current density was identically zero because the electrical potentials at $\theta = 0^\circ$ and $\theta = 36^\circ$ were identical. However, within the finite element model, very small current densities (approximately less than 5 percent of J_z and J_R in the θ direction) were evident. This amount of error is expected for the relatively simple interpolation functions chosen. Increased numerical resolution can be achieved by finer discretization in areas of expected high gradient variation and the possible introduction of higher order interpolation functions for the finite elements.

CONCLUSIONS

The three-dimensional current density structure in the nearfield of an iron-copper galvanic structure was characterized by finely measured SVEI's at incremental positions in an electrolyte in space at $Z = 650 \mu\text{m}$ and $Z = 1125 \mu\text{m}$ above the electrode surface. A corresponding finite element current density field was calculated for positions in space similar to those that were measured. Three-dimensional current density vectors $J(J_x, J_y, J_z)$ were calculated, measured, and subsequently plotted (figures 11 through 15) to create a point-by-point comparison of vector variables in electrolytic space. The comparison, component-versus-component, was in excellent agreement for this relatively simple galvanic configuration.

Based on the completed experimental electric field scans and the corresponding finite element field predictions, it appears that the finite element technique presents a strong analytical tool for calculating the nearfield electric intensity distributions around active electrode surfaces in homogeneous media. The finite element model described in this report made reference to an "a priori" measured set of uncoupled nonlinear polarization curves for pure iron and pure copper (figure 8). With a local tangent slope definition of the potential difference at a given position of the electrode surface, the current densities were calculated everywhere within the electrolyte and on the boundaries.

The measurement technique described has introduced an innovative method for providing a careful comparison with theory in the very nearfield of active galvanic cells. Further advances could lead to a method for predicting the onset of crevice corrosion and pitting in field situations.

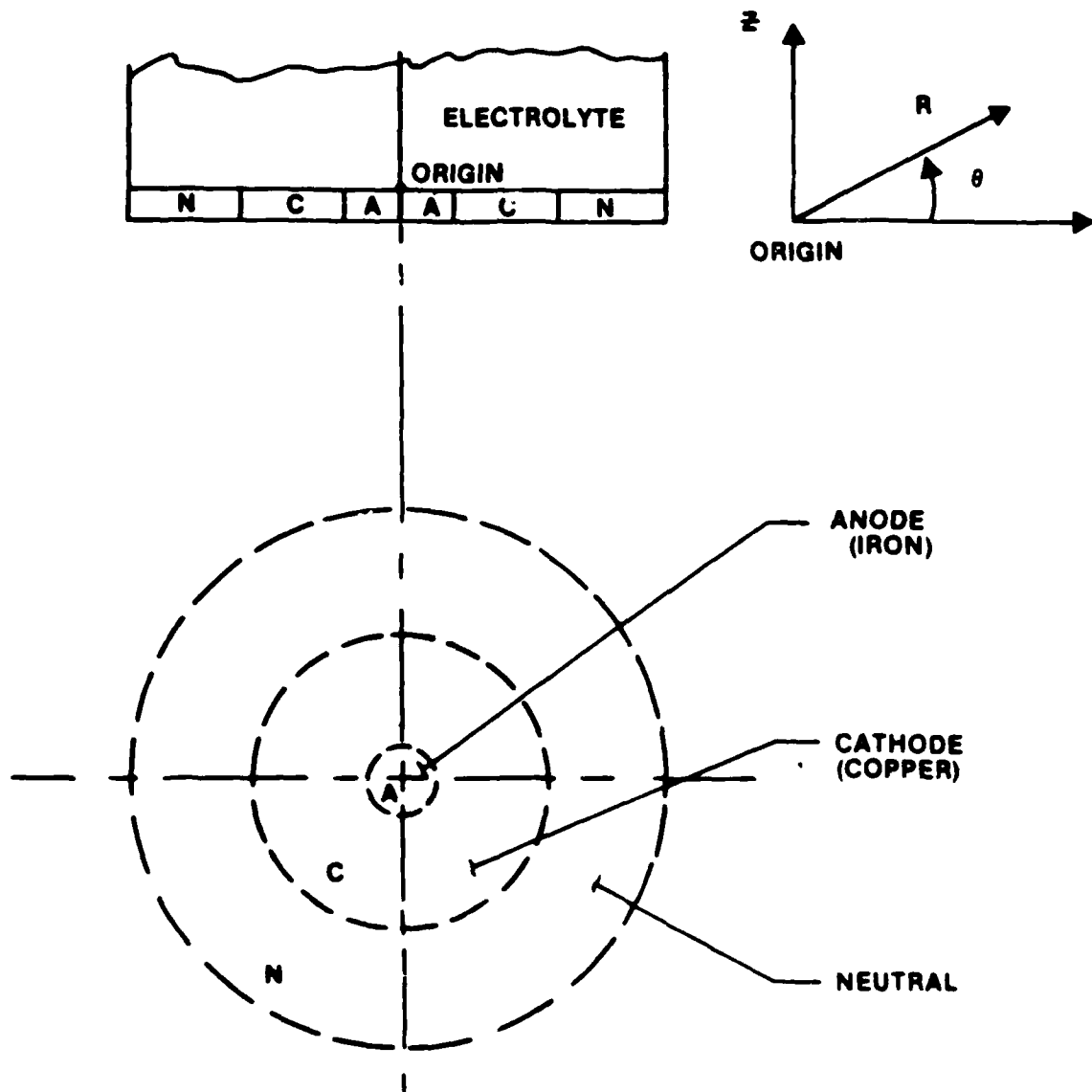


Figure 1. A Schematic of the Iron-Copper Galvanic Couple

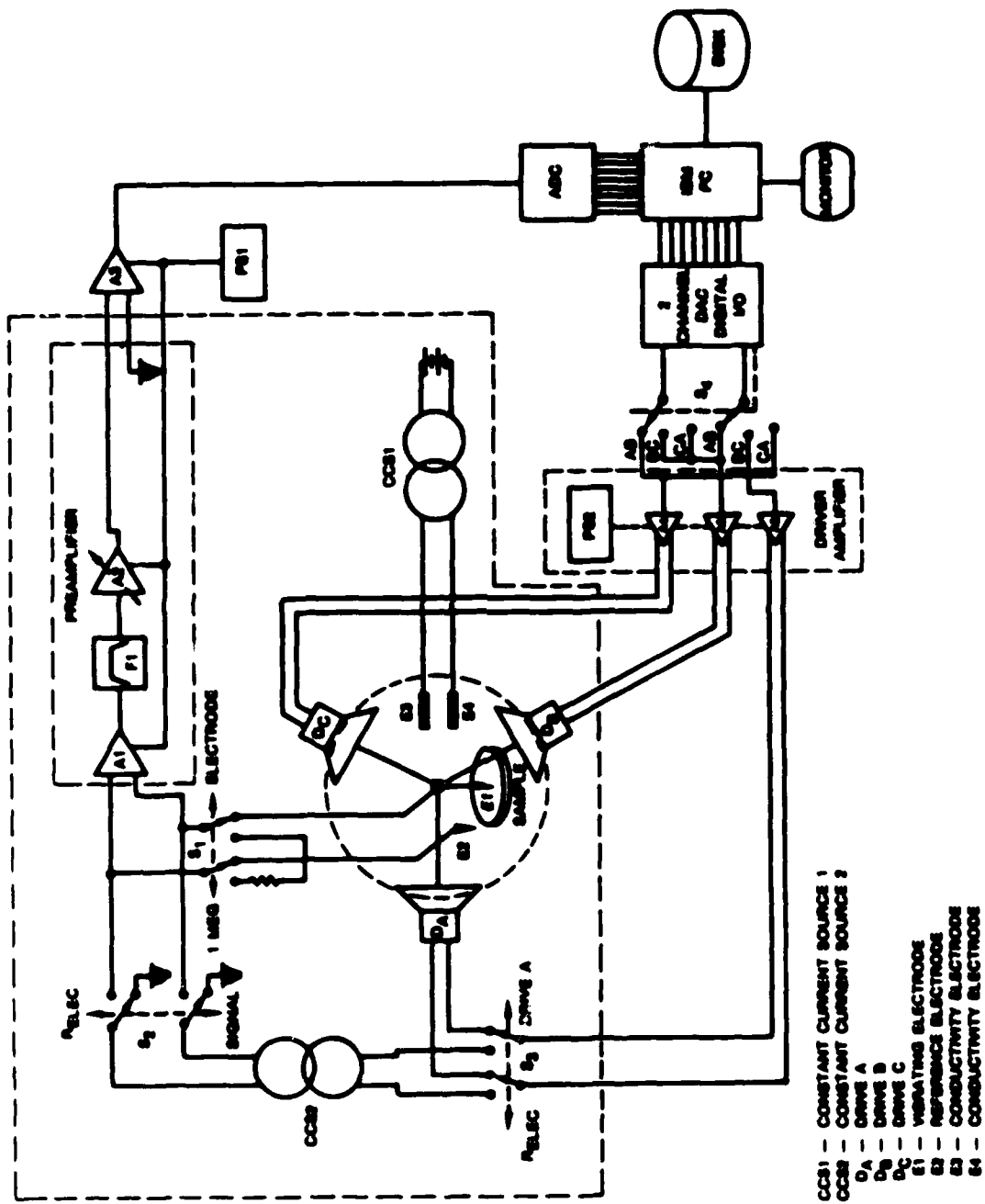


Figure 2. A Schematic of the Three-Dimensional Vibrating Probe

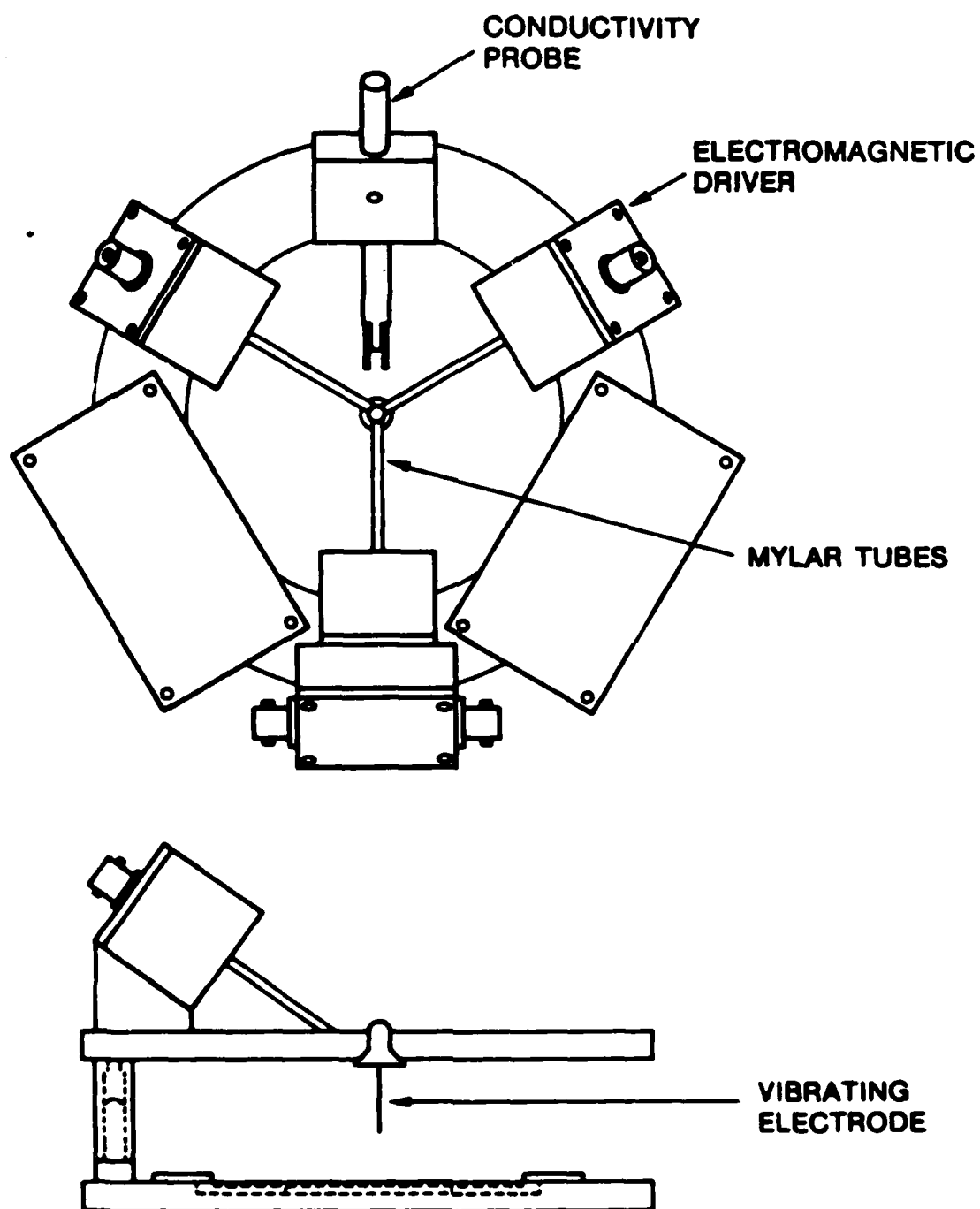


Figure 3. Arrangement of the Probe Components

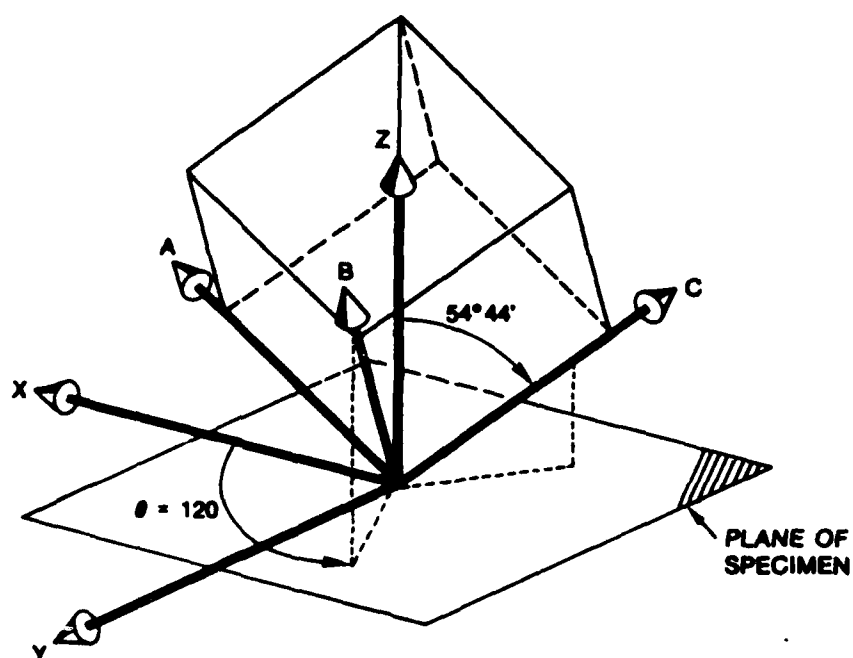


Figure 4. The Relationship Between the X-Y-Z Specimen Coordinate System and the A-B-C Probe Drive Coordinate System

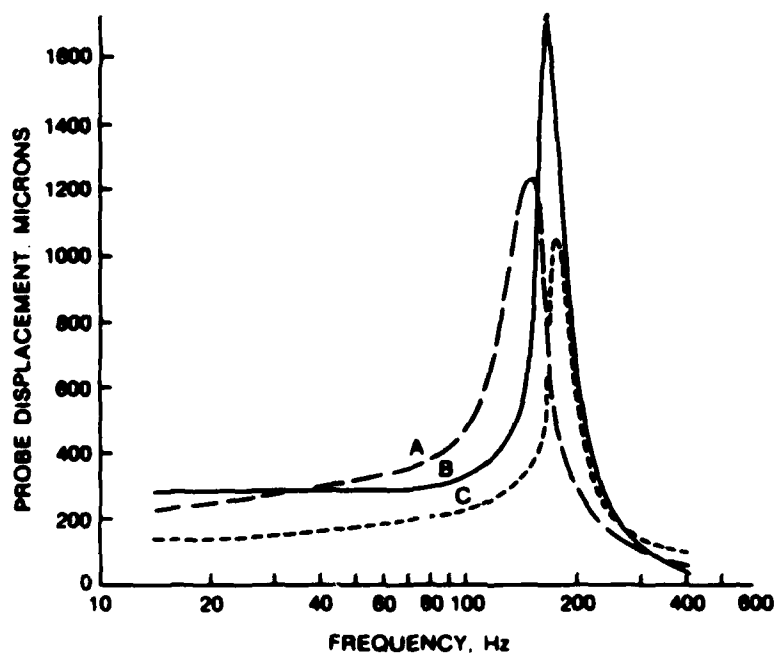


Figure 5. The Frequency Response of the Probe Drivers

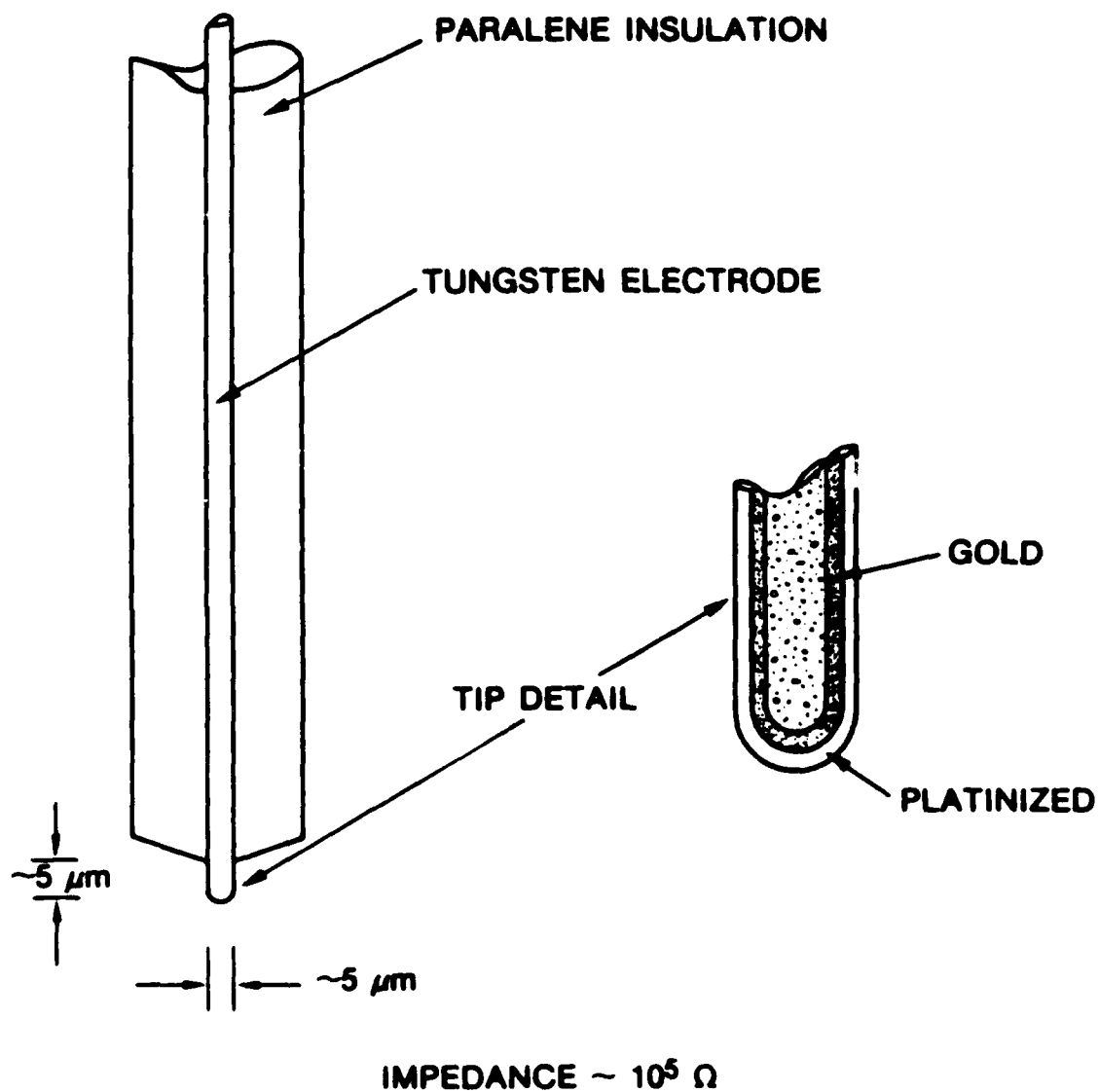


Figure 6. Schematic of the Probe Tip

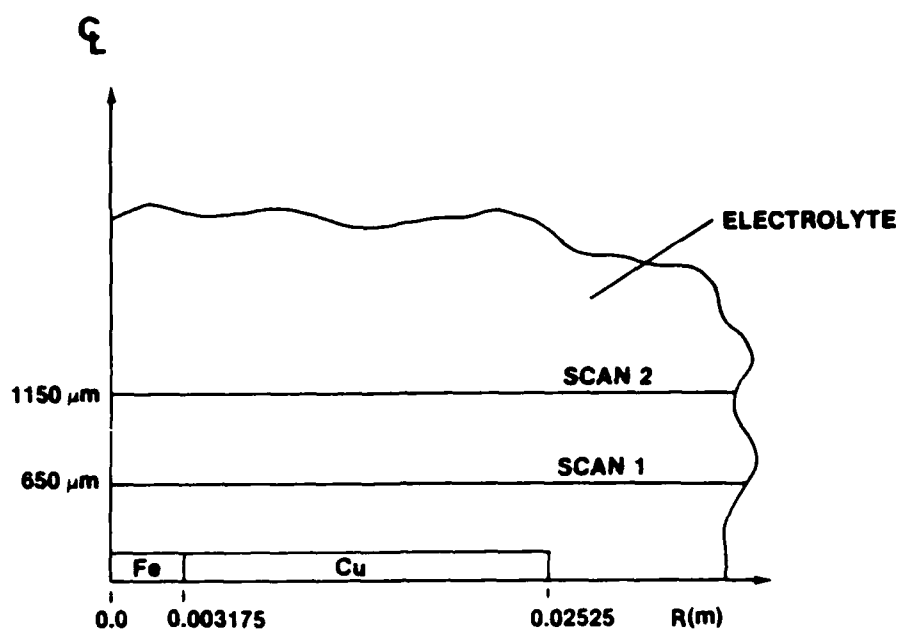


Figure 7. The Geometric Arrangement of the Three-Dimensional Scans

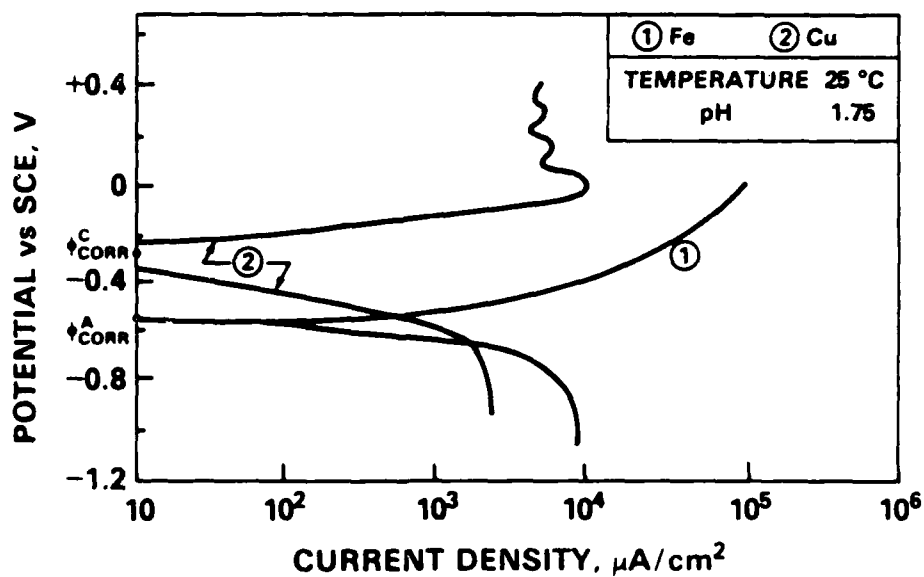
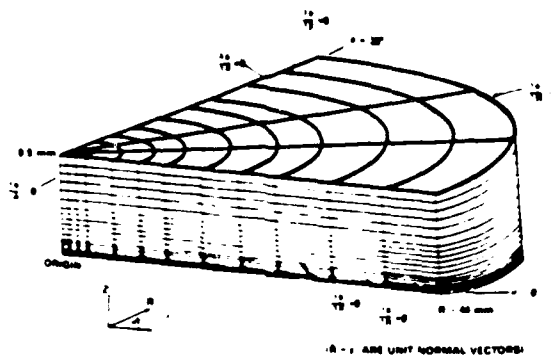


Figure 8. Potentiostatic Polarization Curves for the Iron and Copper Constituents of the Galvanic Couple



BOUNDARY CONDITIONS OF
THE THREE-DIMENSIONAL
FINITE ELEMENT MESH (36°)

(a)

NONLINEAR SOLUTIONS TO:

$$\nabla \cdot \sigma \nabla \Phi = - \frac{\partial \rho}{\partial t} \quad (1)$$

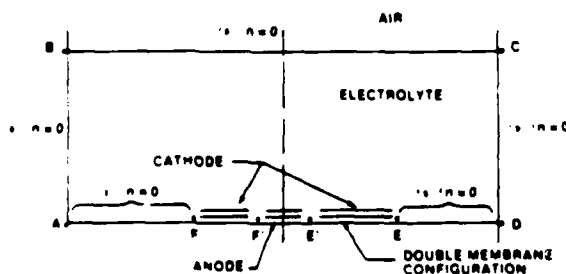
$$\bar{J} = -\sigma \nabla \Phi \quad (2)$$

WHERE

- σ = CONDUCTIVITY (S/m)
- \bar{J} = CURRENT DENSITY (A/m²)
- Φ = POTENTIAL (VOLTS)
- ρ = CHARGE DENSITY (C/m³)
- t = TIME (s)
- ∇ = DEL OPERATOR

USING MEASURED CONSTITUENT
POLARIZATION CURVES

(b)



BOUNDARY CONDITIONS OF MODELED
ELECTROCHEMICAL SPACE

(c)

Figure 9. Summary of the Finite Element Model: Geometric Description, Fundamental Electrical Laws, and Boundary Conditions

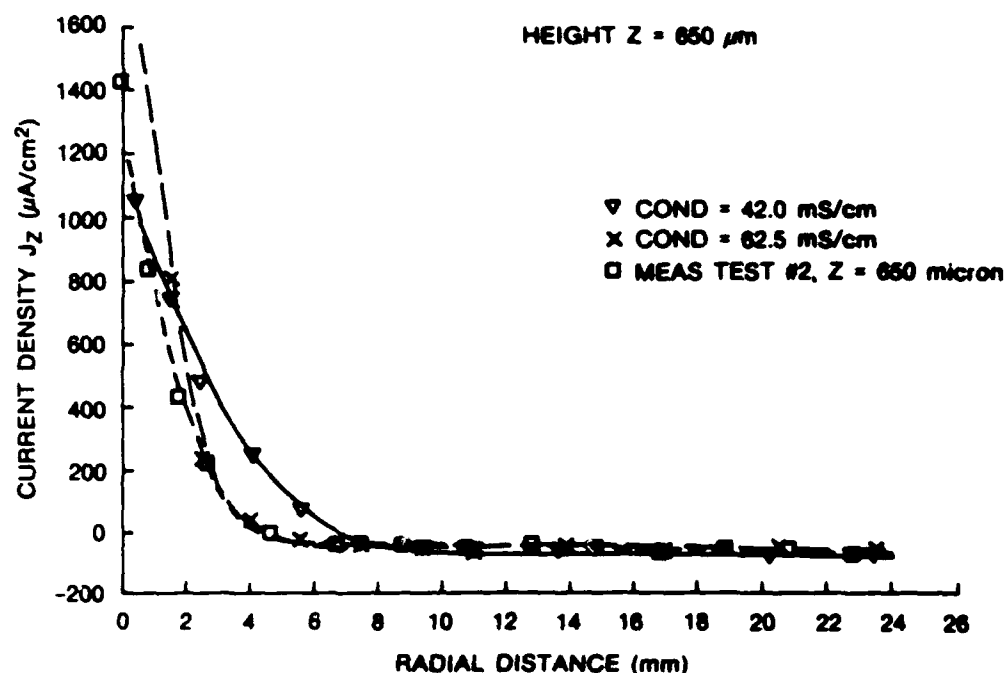


Figure 10. Calculated and Measured J_z Components of the Ionic Current Density at 650- μm Elevation

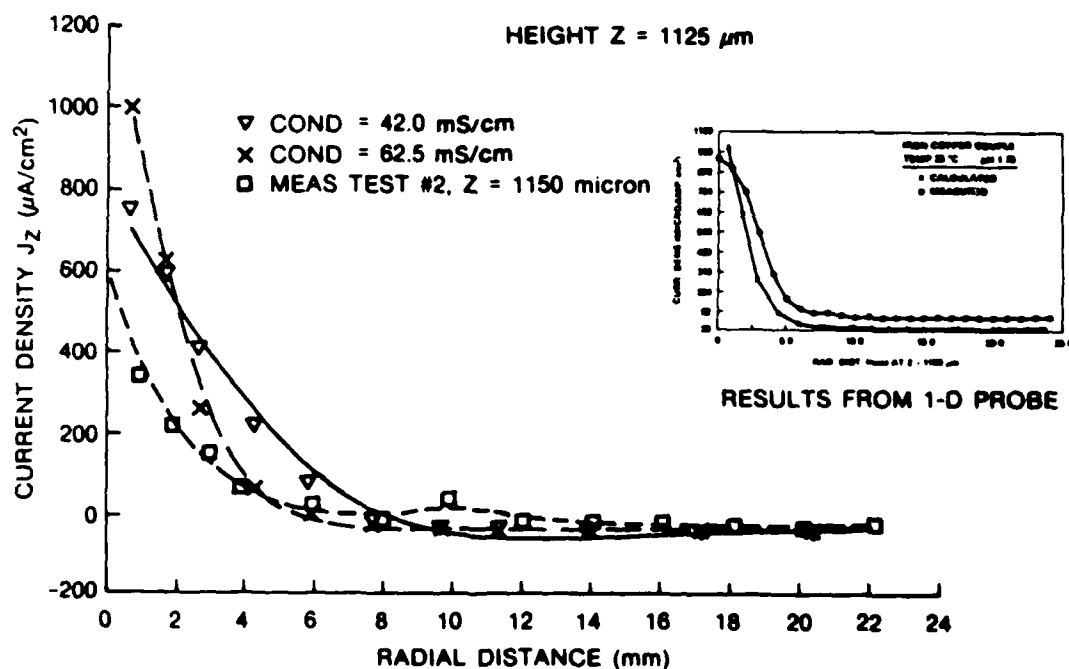


Figure 11. Calculated and Measured J_z Components of the Ionic Current Density at 1125- μm Elevation (Measurement at 1150 μm)

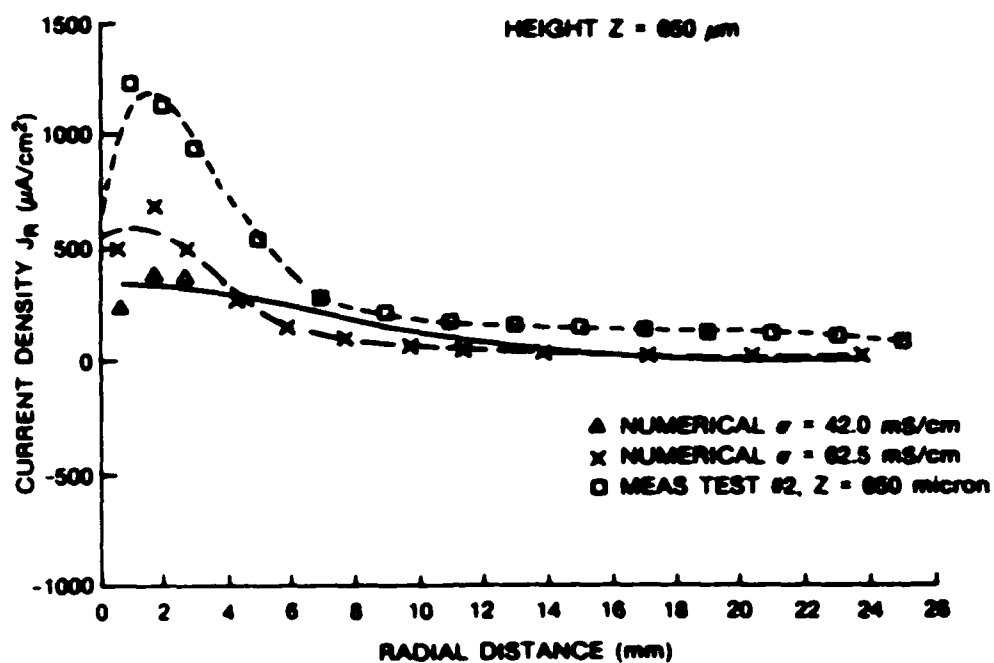


Figure 12. Calculated and Measured J_R Components of the Ionic Current Density at 650- μm Elevation

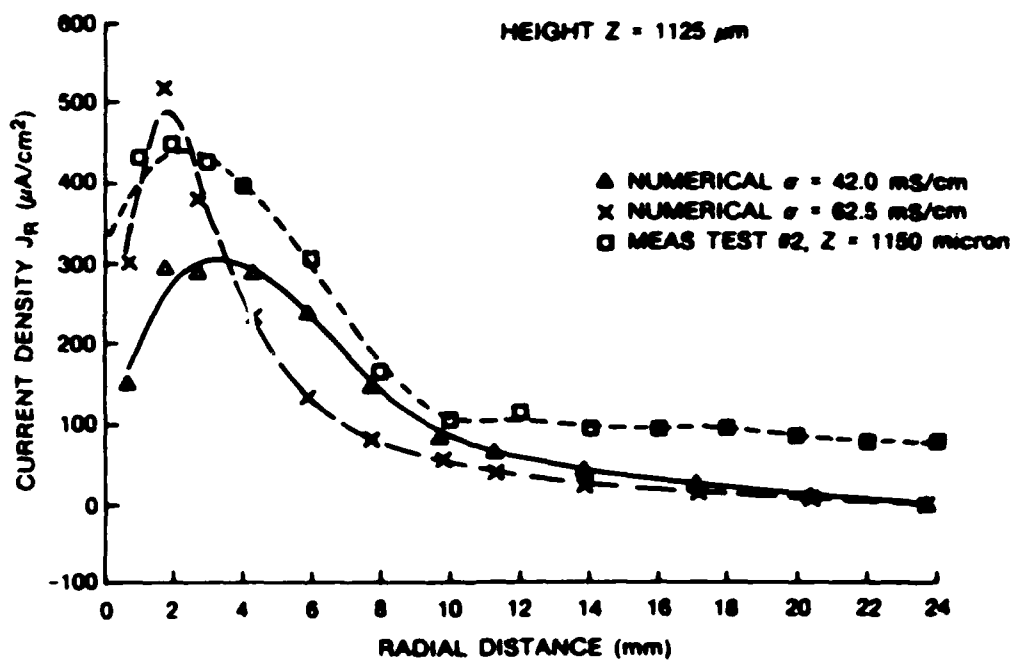


Figure 13. Calculated and Measured J_R Components of the Ionic Current Density at 1125- μm Elevation (Measurements at 1150 μm)

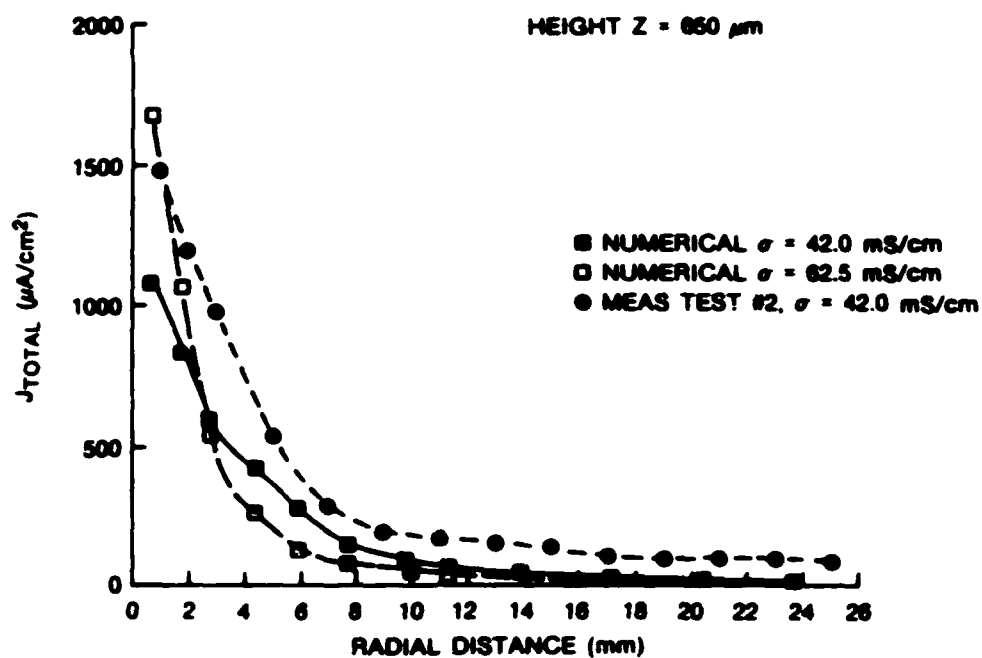


Figure 14. Calculated and Measured Total Ionic Current Density at 650- μm Elevation

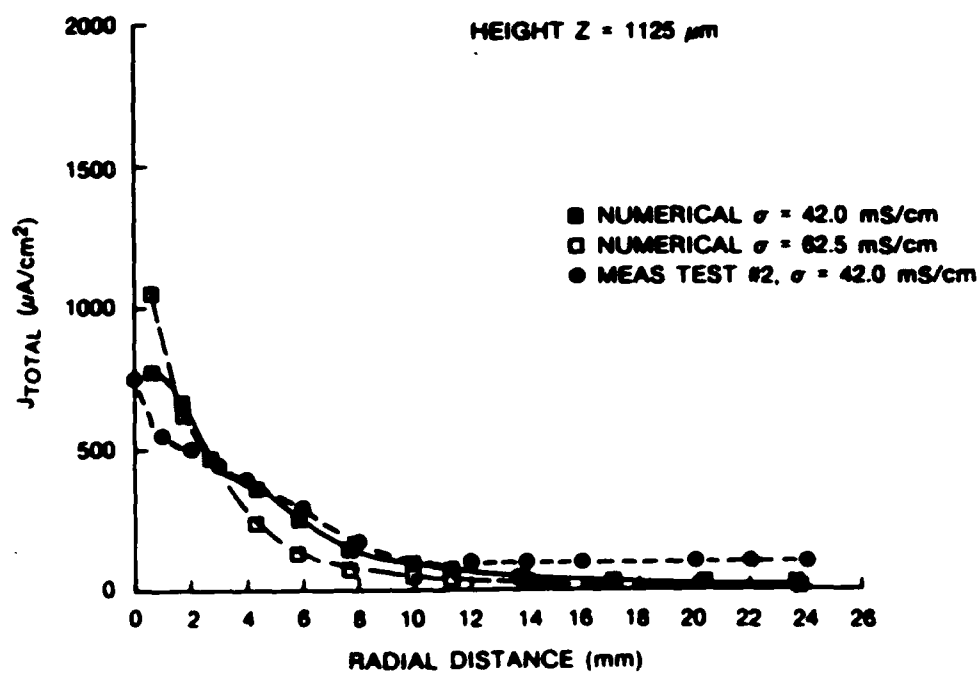


Figure 15. Calculated and Measured Total Ionic Current Density at 1125- μm Elevation (Measurements at 1150 μm)

REFERENCES

1. C. Wagner, Die Chemische Reaktion der Metalle Handbuch der Metallphysik J, Akademische Verlagsgesellschaft Becker und Erler Kom.-Ges., vol. 2, Leipzig, East Germany, 1940, p. 165.
2. K. J. Vetter, Electrochemical Kinetics, Theoretical and Experimental Aspects, Academic Press, Inc., NY, 1967, p. 745.
3. C. Wagner, "Theoretical Analysis of the Current Density Distribution in Electrolytic Cells," Journal of the Electrochemical Society, vol. 98, no. 3, 1951, p. 116.
4. C. Wagner, "Contribution to the Theory of Cathodic Protection," Journal of the Electrochemical Society, vol. 99, no. 1, 1952, p. 1.
5. J. T. Waber, "Mathematical Studies on Galvanic Corrosion I: Coplanar Electrodes With Negligible Polarization," Journal of the Electrochemical Society, vol. 101, no. 6, 1954, p. 271.
6. J. T. Waber, "Mathematical Studies on Galvanic Corrosion II: Coplanar Electrodes With One Electrode Infinitely Large and With Equal Polarization Parameters," Journal of the Electrochemical Society, vol. 102, no. 6, 1955, p. 344.
7. J. T. Waber, "Mathematical Studies on Galvanic Corrosion VI: Limiting Case of Very Thin Films," Journal of the Electrochemical Society, vol. 103, no. 10, 1956, p. 567.
8. E. McCafferty, "Distribution of Potential and Current in Circular Corrosion Cells Having Unequal Polarization Parameters," Journal of the Electrochemical Society, vol. 124, no. 12, 1977, p. 1869.
9. R. Alkire, T. Berhg, and R. L. Sani, "Predicting Electrode Shape Change With Use of Finite Element Methods," Journal of the Electrochemical Society, vol. 125, no. 12, 1978, p. 1980.
10. R. Alkire and D. Sitarl, "The Location of Cathodic Reaction During Localized Corrosion," Journal of the Electrochemical Society, vol. 126, no. 15, 1979, p. 15.
11. J. W. Fu, "A Finite Element Analysis of Corrosion Cells," Corrosion, vol. 38, no. 5, 1982, p. 295.
12. R. S. Munn, "A Mathematical Model for a Galvanic Anode Cathodic Protection System," Materials Performance, vol. 21, no. 8, August 1982, p. 29.
13. R. G. Kasper and M. G. April, "Electrogalvanic Finite Element Analysis of Partially Protected Marine Structures," CORROSION/82, Houston, TX, 22-26 March 1982.

REFERENCES (Cont'd)

14. H. P. E. Helle, G. H. M. Beek, and J. T. Ligtelign, "Numerical Determination of Potential Distributions and Current Densities in Multi-Electrode Systems," CORROSION, vol. 37, no. 9, 1981, p. 522.
15. R. G. Kasper and M. O. Duffy, Mathematical Models of Nonlinear Galvanic Polarization, NUSC Technical Report 6921, Naval Underwater Systems Center, New London, CT, 16 August 1983.
16. R. S. Munn, "Using the MARC Finite Element Computer Program for Numerical Analysis of Galvanic Systems for Marine Cathodic Protection System Design," MARC User's Symposium, Palo Alto, CA, October 1982.
17. Y. Ishikawa and H. S. Issacs, The Study of Pitting Corrosion of Aluminum by Means of the Scanning Vibrating Electrode Techniques, BNL Report No. 33059, Brookhaven National Laboratory, Brookhaven, NY, 1983.
18. C. R. Crowe, "Localized Corrosion Currents From Graphite/Aluminum and Welded SiC/Al Metal Matrix Composites," NRL Memorandum Report, Naval Research Laboratory, Washington, DC (In Process).
19. C. R. Crowe, "Localized Ionic Currents From a Corroding Iron-Copper Galvanic Couple," NRL Memorandum Report, Naval Research Laboratory, Washington, DC (In Process).
20. C. R. Crowe and R. G. Kasper, "Ionic Current Densities in the Nearfield of a Corroding Iron-Copper Galvanic Couple," Journal of the Electrochemical Society, vol. 133, no. 5, 1986.
21. L. A. Geddes, Electrodes and Measurement of Bioelectric Events, Wiley-Interscience, New York, 1972, p. 147.

INITIAL DISTRIBUTION LIST

Addressee	No. of Copies
DTIC	12
ONR (Code 431)	3
NRL (Code 6000, -6300, -2627, -6372 (Dr. C. R. Crowe))	3
NADC (Code 606 (Dr. J. DeLuccia))	1
NSWC, White Oak (Library)	1
NOSC (Library)	1
NPS (Mech Eng Dept (Dr. D. H. Boone))	1
NAIR (Code 310A, -5304B)	2
NAVSEA (Code 05R)	1
Naval Air Propulsion Ctr (Library)	1
Naval Electronics Lab (Electron Mat'ls Science Div)	1
Naval Missile Ctr (Code 3312-1 (Mat'ls Consultant))	1
Naval Construction Battalion (Mat'ls Div)	1
DTNSRDC, Carderock	1
NWC (Library)	1
NASA (Library)	1
NBS (Metals Science and Stand Div, Ceramic Glass and Solid State Science Div, Fracture and Deformation Div)	3
NFAC (Code 03)	1
USMC (Code AX (Scientific Advisor))	1
Army Research Office (Metallurgy & Ceramics Program)	1
Army Materials & Mechanics Research Ctr (Research Programs Office)	1
Air Force Office of Scientific Research/NE (Electronics & Materials Science Directorate)	1
NASA Headquarters (Code RRM)	1
National Academy of Sciences (ONR Representative (M. T. McCracken))	1
Battelle Memorial Institute (Defense Metals and Ceramics Info Ctr)	1
Oak Ridge Nat'l Lab (Metals and Ceramics Div)	1
Los Alamos Scientific Lab (Report Librarian)	1
Argonne National Lab (Metallurgy Div)	1
Brookhaven Nat'l Lab (Technical Info Div)	1
Lawrence Radiation Lab (Library)	1
Carnegie-Mellon Univ (Prof. I. M. Bernstein)	1
Univ of Illinois (Prof. H. K. Birnbaum)	1
Rensselaer Polytechnic Inst (Prof. D. J. Duquette)	1
Ohio State Univ (Prof. J. P. Hirth, Prof. B. E. Wilde)	2
Lehigh Univ (Prof. H. Leidheiser, Jr., Prof. R. P. Wei)	2
Rockwell International Science Ctr (Dr. F. Mansfeld)	1
Univ of Pittsburgh (Prof. G. H. Meier, Prof. F. S. Pettit)	1
Martin Marietta Lab (Dr. J. R. Pickens)	1
Penn State Univ (Prof. H. W. Pickering)	1
Michigan State Univ (Prof. R. Summit)	1
Univ of Calif (Prof. A. J. Ardell)	1
SUNY (Dr. C. R. Clayton)	1

END

4-87

DTIC